



# Identification of damage severity in *Fraxinus excelsior* L. trees caused by ash dieback using multisensory and multitemporal UAV imagery

Lisa Buchner <sup>\*</sup>, Anna-Katharina Eisen, Susanne Jochner-Oette

Physical Geography / Landscape Ecology and Sustainable Ecosystem Development, Catholic University of Eichstätt-Ingolstadt, Eichstätt 85072, Germany

## ARTICLE INFO

### Keywords:

Common ash  
*Hymenoscyphus fraxineus*  
Multispectral  
RGB  
Thermal  
Thresholding  
Vegetation indices

## ABSTRACT

The extended spread of ash dieback in Europe has far-reaching consequences for *Fraxinus excelsior* L. populations. The progression of the disease leads to characteristic symptoms, particularly within the tree crowns. To date, assessing the damage severity of each individual tree typically requires in-field inspections. However, UAVs equipped with RGB, thermal, and multispectral sensors offer cost-effective and objective possibilities. This study relied on such analyses and focused on two ash seed orchards in Baden-Wuerttemberg, Germany, where visual inspections were compared with multisensorial data obtained in spring, summer and autumn of 2022 and 2023. The calculated RGB and multispectral vegetation indices were able to significantly discriminate between different degrees of damage due to ash dieback; in contrast, thermal data were less reliable and linked to different dynamics. Novel thresholds applied to the vegetation indices enabled a classification of mild and severe damage with an overall accuracy of 74.9 % for the multispectral index DVI (Difference Vegetation Index) and 73.0 % for the RGB index GRVI (Green-Red Vegetation Index). Combining RGB and multispectral indices further improved the overall accuracy to 77.2 %. The presented workflow offers forest practitioners an accessible toolset for evaluating the health status of ash populations affected by ash dieback.

## 1. Introduction

The common ash (*Fraxinus excelsior* L.) in Europe is seriously threatened in its existence due to the ash dieback disease caused by the invasive fungal pathogen *Hymenoscyphus fraxineus* (T. Kowalski) Baral, Queloz, Hosoya (Baral et al., 2014). Since the first documentation of ash dieback in Poland in the 1990s (Kowalski, 2006, Timmermann et al., 2011), the disease has become increasingly widespread across Europe, causing extensive damage to ash populations. Infected trees present typical symptoms of dying shoots and increased leaf loss with thinning of the crowns. Especially in more severely damaged trees, epicormic shoots often constitute a large part of the remaining foliage. Ash dieback is linked to a high mortality rate amongst the affected trees (Enderle et al., 2019), and the European ash populations are expected to drastically decrease over the next few decades (Coker et al., 2019). In Germany, the European common ash is a common tree species both in forests and non-forest sites, such as private gardens, along rivers or in public spaces (Enderle et al., 2017a). In 2022, the fourth National Forest Inventory documented that ash accounted for 1.8 % of Germany's total forest area (BMEL, 2024). As an ecologically vital tree species, with

several species dependent on the existence of the common ash, its conservation is crucial in the face of ash dieback (Mitchell et al., 2017, Hultberg et al., 2020). Additionally to the high ecological impact, the common ash is also an important economic tree species, as it is also valued for its high-quality timber (Pautasso et al., 2013). However, symptoms of ash dieback can also manifest as collar and root rot, negatively influencing the stability of the affected trees. Those trees present a safety risk for humans (e.g., forest workers or visitors) and infrastructure (e.g., traffic roads) (Metzler and Herbstritt, 2014, Enderle et al., 2017b, Skovsgaard et al., 2017). The vast majority of ash trees in German forest stands has been affected by ash dieback, with only very few healthy trees remaining (Fuchs et al., 2024). To assess the damage severity and gain an estimate of the health status of ash populations, usually each individual tree has to be assessed by a trained expert in the field. Rating scales are commonly used to classify trees into classes based on their health, taking into account various factors such as foliage density or the presence of epicormic shoots (Lenz et al., 2012, Peters et al., 2021).

Remote sensing technologies offer advantageous options for forest monitoring. Unmanned aerial vehicles (UAVs) equipped with a variety

\* Corresponding author.

E-mail address: [LBuchner@ku.de](mailto:LBuchner@ku.de) (L. Buchner).

<https://doi.org/10.1016/j.foreco.2025.122660>

Received 17 December 2024; Received in revised form 6 March 2025; Accepted 9 March 2025

Available online 22 March 2025

0378-1127/© 2025 The Authors. Published by Elsevier B.V. This is an open access article under the CC BY license (<http://creativecommons.org/licenses/by/4.0/>).

of different sensor systems allow for the rapid assessment of large areas. UAVs have been tested in a number of forest applications, e.g., for the estimation of tree parameters, species phenotyping, phenology, drought stress, fire hazards, nutrient status, insect pests and plant diseases (Torresan et al., 2017, Barbedo, 2019, Abd El-Ghany et al., 2020, Kleinsmann et al., 2023). Plant stress caused by biotic and abiotic factors can be detected using UAV technology (Castro et al., 2021). Sensors such as RGB, thermal, as well as multi- and hyperspectral UAV systems provide valuable insights into plant disease status (Neupane and Baysal-Gurel, 2021). The foliage of each plant is linked to a specific spectral reflectance, and the analysis thereof gives indications on the plant's biochemical components and overall health. Vegetation indices (VIs), calculated by formulas that commonly incorporate multiple wavelengths are often employed to analyse the spectral reflectance (Huete, 2012).

Inexpensive RGB sensors can provide information on plant height and crown diameter (Barbosa et al., 2021), biomass (Bendig et al., 2015), phenology (Park et al., 2019), canopy area (Starý et al. 2020) or forage yield (Lussem et al., 2018). Especially in the context of plant diseases, VIs based on RGB data have been proven to be a valuable tool for the identification and characterization of damage caused by plant diseases. Diseases can cause subtle changes in leaf colour, texture, and brightness, making RGB VIs effective for identifying diseases early, even before symptoms become visually severe. For example, a significant relationship between different RGB VIs and leaf rust severity was documented for wheat (*Triticum aestivum* L.) affected by the fungus *Puccinia triticina* (Bhandari et al., 2020). Similarly investigations on diseased citrus trees also proved a connection between RGB VIs and health status (Garza et al., 2020). Using RGB VIs, it was also possible to detect disease severity in rice (*Oryza* spp.) caused by narrow leaf spot (Cai et al., 2018).

With more specific wavelengths, also extending to the red-edge and near-infrared range, multispectral sensors offer a wide range of additional information to the visible light sensors. Multispectral UAV data are widely used in various applications such as precision farming (Candiago et al., 2015) and can also effectively identify and monitor physiological stress in trees (Dash et al., 2017). Healthy and diseased trees often display distinct spectral signatures, influenced by differences in pigment composition and structural properties (Mahlein et al., 2013). Numerous multispectral VIs exist, each targeting specific wavelengths with a focus on characteristics such as biomass, greenness, or vegetation status (Xue and Su, 2017). In the context of plant diseases, multispectral data have been shown to be successful in identifying diseases. UAV multispectral data in combination with VIs were used to detect grapevine (*Vitis vinifera* L.) disease (Albetis et al., 2017), monitor sugarcane white leaf disease symptoms (Sanseechan et al., 2019) and detect banana (*Musa* spp.) plant diseases (Ye et al., 2020, Choosumrong et al., 2023).

Thermal sensors, which capture the surface temperature including those of plants, offer unique possibilities for detecting plant diseases and the overall health status of plants (Hashim et al., 2020). Disease induced stress can lead to the closure of leaf stomata, reducing the transpiration rate and resulting in higher leaf temperatures. Increased plant surface temperatures were often observed using thermal imaging techniques even before visible symptoms were documented (Chaerle et al., 1999, Jafari et al., 2017, Ortiz-Bustos et al., 2017). For instance, thermal imaging successfully identified diseases in banana plants (Anasta et al., 2021), and significant differences in leaf surface temperature were observed in oilseed rape (*Brassica napus*) infected with fungal species of the genus *Alternaria* (Baranowski et al., 2015).

In the context of plant diseases, thermal imaging has mostly been carried out under controlled indoor conditions, since thermal systems can be easily influenced by outdoor conditions, such as changing solar conditions or wind (Hashim et al., 2020). Nevertheless, UAVs equipped with thermal cameras have also proven to be valuable tools to identify plant disease status. Smigaj et al. (2015) investigated the use of a

UAV-operated thermal camera to monitor the canopy temperature of diseased trees and were able to document a significant positive correlation between tree canopy temperature and disease status.

While the use of UAVs in forests or plantations to detect plant diseases is widespread (Holzwarth et al., 2023), few studies using remote sensing technologies have focused on ash tree health: The impact of the emerald ash borer (*Agrilus planipennis*), a major insect pest additionally threatening ash populations, on ash tree health has been assessed using hyperspectral data (Pontius et al., 2008) and multispectral WorldView-2 satellite data (Murfit et al., 2016). Both data enabled an estimation of the health status of the affected ash trees. Waser et al. (2014) also used WorldView-2 data and calculated multispectral VIs for classifying four different levels of damage caused by ash dieback. Hyperspectral data facilitated the identification of individual ash trees affected by ash dieback (Chan et al., 2021, Polk et al., 2022). Further, Kampen et al. (2019) demonstrated the potential of UAV-based multispectral data to assess ash dieback severity.

However, none of the studies integrated thermal sensors or are partly only based on single seasons and years. Moreover, the results of the few studies focusing on the damage caused by ash dieback reported difficulties in detecting the damage severity and complex workflows make it difficult to implement these in practice across the board.

Therefore, this study investigates the potential of RGB, multispectral and thermal UAV surveys to determine the extent of damage to *Fraxinus excelsior* L. affected by ash dieback in two German ash seed orchards. We hypothesize that vegetation indices values derived from UAV surveys vary based on infection status. Additionally, the use of thresholds may effectively differentiate between varying degrees of damage. Multiple UAV surveys spread over the course of two years (2022–2023) provide extensive data at different times of the vegetation period. Emphasis is placed on the effectiveness of the three different camera systems. Practical applications for forest practitioners are a key focus of this study, since the fast and straightforward use of UAV systems combined with an easy-to-follow workflow can enable a quick estimate of the disease status of ash populations.

## 2. Materials and methods

### 2.1. Study sites

This study was conducted at two study sites (Fig. 1), located in the south of Germany in the federal state of Baden-Wuerttemberg. Both study sites have previously been included in research on ash dieback (Enderle et al., 2015, Buchner et al., 2022, Buchner et al., 2024, Eisen et al., 2024), thus detailed information on the health status of the planted individuals already exists.

The ash seed orchard Emmendingen (48°6'38.50"N, 7°52'20.49"E, 209 m NHN) is located approx. 15 km north of the city Freiburg. The plantation has a size of 2.7 ha and was established in 1995. Originally, 228 ash trees were planted in a grid of 10 m x 10 m. Even though there were no thinning measures, 142 trees had to be removed due to ash dieback, with only 86 ash trees consisting of 32 different genotypes remaining.

The seed orchard Schorndorf (48°46'35.59"N, 9°25'31.00"E, 420 m NHN) is located east of the state capital Stuttgart in Baden-Wuerttemberg. The plantation was established in 1992 with a spacing of 7 m x 7 m and has an area of approx. 2.27 ha. 416 ash trees were originally planted, but since then, due to thinning measures and the effect of ash dieback, 296 of the ash trees were removed and only 120 living trees, consisting of 30 different genotypes remained on the orchard.

### 2.2. Methods

Fig. 2 provides an overview of the applied workflow of the UAV surveys, the respective post-processing of the data and the workflow for

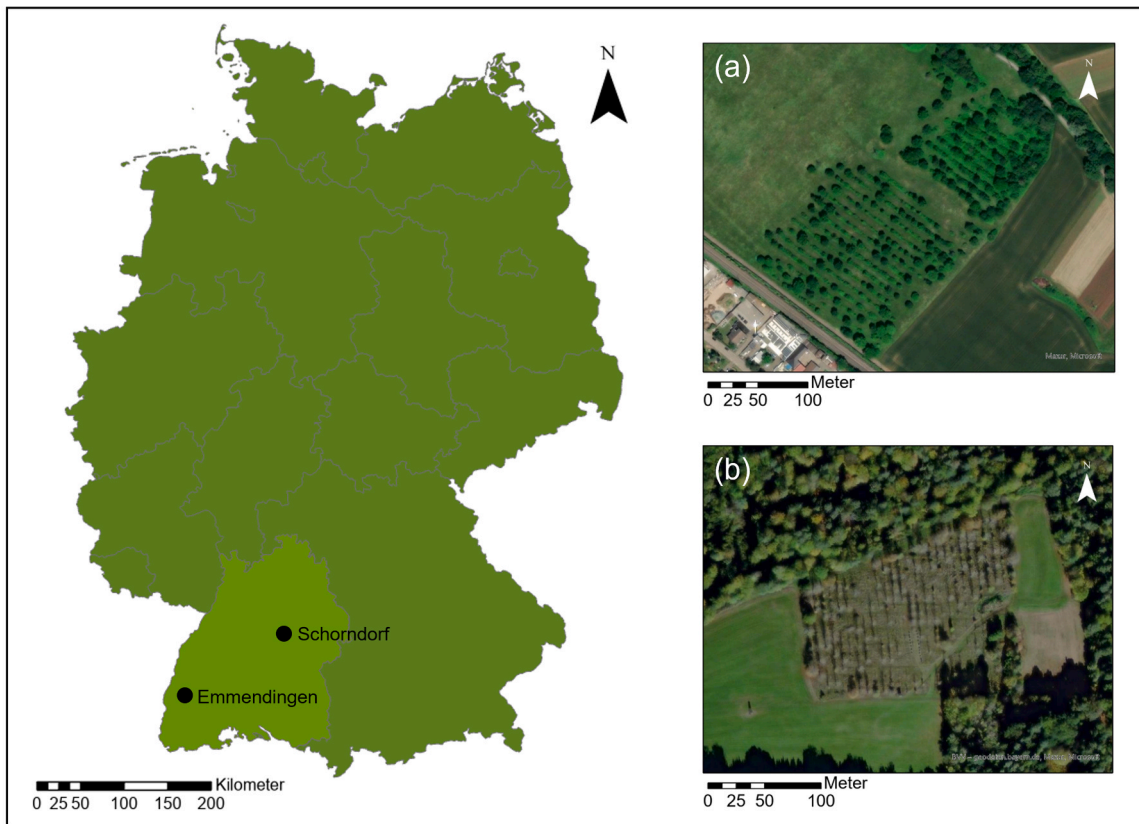


Fig. 1. Study sites Emmendingen (a) and Schorndorf (b) located in the federal state of Baden-Wuerttemberg (light green) in Germany (green), Source: Esri Base Map.

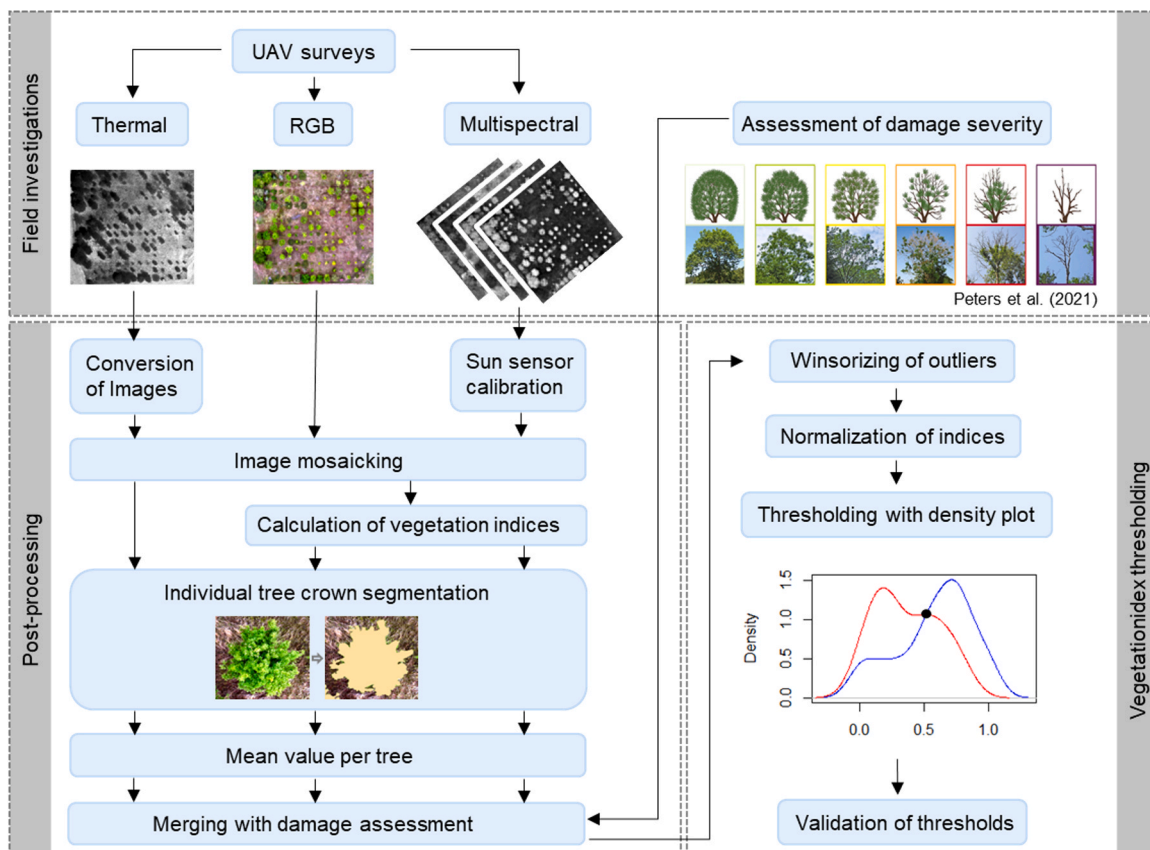


Fig. 2. Methodological framework of the field investigations, post-processing of the data and the vegetation index thresholding.

obtaining and analysing vegetation indices to index thresholding. In brief, the multisensorial vegetation indices were calculated for each tree and compared with field-based vitality assessments to evaluate the index's effectiveness in distinguishing different levels of damage. Differences across vitality classes were tested for statistical significance, using appropriate statistical methods based on data distribution and variance. This approach was used to identify suitable indices for assessing damage severity. A key advancement of this study is represented by the calculation of thresholds that can be universally used in assessing the ash tree's health based on remotely sensed data following this workflow. The individual work steps are explained in more detail in the following.

### 2.2.1. Assessment of vitality

Each of the ash trees on both ash seed orchards was assessed regarding their vitality, by using a standardized vitality scoring systems developed by Peters et al. (2021). The ash trees were classified into six categories, ranging from class 0, consisting of healthy trees, to mildly damaged trees (class 1 and 2), severely damaged trees (class 3 and 4) and lastly to dead trees (class 5). Each class is characterised by different degrees of thinning of the crown, leaf loss, dead shoots and branches, and the presence of epicormic shoots. The vitality assessments were conducted at both orchards in late July of 2022 and 2023.

### 2.2.2. UAV surveys

**2.2.2.1. Image acquisition.** Between spring and autumn in 2022 and 2023, two to four UAV aerial surveys were conducted at each study site (Table 1). Two UAV systems were employed: the DJI Mavic 2 Enterprise Advanced (Mavic 2 EA) and the DJI Mavic 3 Multispectral (Mavic 3 M). The Mavic 2 EA is equipped with a 48 MP RGB camera and a thermal sensor, capturing both RGB and thermal images simultaneously. The Mavic 3 M, on the other hand, features a 20 MP RGB camera and four 5 MP multispectral sensors, which record multispectral and RGB images concurrently. The multispectral sensors cover the near-infrared (860 nm ± 26 nm), red edge (730 nm ± 16 nm), red (650 nm ± 16 nm), and green (560 nm ± 16 nm) wavelengths. An integrated sun sensor measures solar radiation, enabling light compensation during image post-processing which enhances the accuracy and consistency of data over time (DJI, 2022).

All surveys were taken at a flight height of 80 m above the ground, with side and front overlaps of 85 % and a flight speed of 3 m/s for the Mavic 2 EA and 4 m/s for the Mavic 3 M. A ground sampling distance of 2.22 cm/pixel was achieved for RGB and 10.48 cm/pixel for thermal images taken by the Mavic 2 EA and 2.77 cm/pixel for the multispectral images of the Mavic 3 M.

Pre-planned flight plans were generated using the UAVs' software to ensure comprehensive coverage of the entire plantation sites. Due to the size of the plantations and the UAVs' battery limitations, each survey was divided into two flight missions at the Schorndorf seed orchard and three at the Emmendingen seed orchard. These consecutive missions were conducted back-to-back to minimize any changes in environmental conditions between flights. All surveys were carried out on sunny, cloud-free days with minimal wind to ensure optimal image quality and consistency.

The images were georeferenced using ground control points (GCPs)

that were represented by red sheets with reflecting panels. The coordinates of the GCPs were recorded using the surveying system Stonex S9III (STONEX® Srl, Paderno Dugnano, Italy). The Mavic 3 M includes an RTK module, ensuring positioning with centimetre precision, and no GCPs were used for those flights.

**2.2.2.2. Image processing of multispectral and RGB data.** RGB and multispectral images captured by the UAV systems were processed using Agisoft Metashape Professional (version 1.8.1). After aligning the imported images, a point cloud was generated, followed by the construction of an orthophoto. For the multispectral images, data from the sun sensor were used for calibration. Georeferencing was achieved with recorded GCPs and, in the case of the Mavic 3 M, supplemented by recorded RTK data.

Subsequently, the orthophotos were imported into ArcGIS Pro (version 2.8.3) and the individual tree crowns were manually delineated. A polygon was created to represent the shape of each tree crown, capturing only leaf mass. Although several methods for automatic single tree crown segmentation exist (Dalponte et al., 2015, Panagiotidis et al., 2017, Mohan et al., 2017, Qiu et al., 2020, Miraki et al., 2021), none achieved the necessary accuracy for this study. Given the generous spacing of ash trees in both orchards, manual segmentation of the crowns was feasible. Since ash dieback causes leaf loss and crown thinning, special care was taken to segment only those areas of the crown that still contained leaves. This approach minimized the influence of extraneous pixels, particularly ground pixels. Some trees were excluded from further analyses due to crown blurring caused by movement of the tree crowns during the UAV survey.

**2.2.2.3. Vegetation indices and thresholding.** RGB band values were first normalized, as described in Eqs. 1 – 3, to reduce the effects of illumination (Torres-Sánchez et al., 2014, Zhang et al., 2019, Suh et al., 2020, Barbosa et al., 2021) using the raster calculator in ArcGIS Pro.

$$r = \frac{R}{R + G + B} \quad (1)$$

$$g = \frac{G}{R + G + B} \quad (2)$$

$$b = \frac{B}{R + G + B} \quad (3)$$

Ten RGB and ten multispectral VIs were selected, each in the context of plant health. The respective VIs and their definitions are listed in Table 2.

Using the raster calculator in ArcGIS Pro, the individual bands of the generated orthophotos were used to calculate the VIs. The zonal statistics tool was then applied to calculate the mean VI value per tree canopy using the segmented tree crown polygons.

The mean vegetation index value for each tree was compared with the field-based vitality assessments to evaluate each index's capability to distinguish between varying levels of ash dieback damage. Statistical differences among the four vitality classes (1–4) were formally assessed using ANOVA. In these models, vegetation index values represented the dependent variables, while the field-assessed vitality class served as the independent categorical factor. Assumptions underlying ANOVA, namely the normality of residuals and homogeneity of variances, were

**Table 1**

Months in which the aerial surveys were conducted in 2022 and 2023 for the two seed orchards Emmendingen and Schorndorf and the used UAVs: Mavic 2 EA (M2EA), Mavic 3 M (M3M).

Seed orchard	2022				2023			
	May	June	July	Oct.	May	June	July	Oct.
Emmendingen	M2EA		M2EA	M2EA		M2EA, M3M	M3M	M2EA, M3M
Schorndorf		M2EA		M2EA	M2EA	M2EA, M3M	M3M	M2EA, M3M

**Table 2**

Vegetation indices (VIs) selected for this study. For each index, the equation and exemplary references, where the VI was applied in the context of plant health, are displayed.

	Vegetation index	Equation	References	
RGB	Green-Red Vegetation Index	$GRVI = \frac{g-r}{g+r}$	(Albetis et al. 2017, Albetis et al. 2019)	
	Excess Green Index	$ExG = 2 * g - r - b$	(Cai et al. 2018)	
	Excess Red Index	$ExR = 1.4 * r - g$	(Cai et al. 2018)	
	Excess Green-Red	$ExGR = ExG - ExR$	(Cai et al. 2018)	
	Green Leaf Index	$GLI = \frac{2 * g - r - b}{2 * g + r + b}$	(Bhandari et al. 2020)	
	Red Green Blue Vegetation Index	$RGBVI = \frac{g^2 - b * r}{g^2 + b * r}$	(Bendig et al. 2015)	
	Red Green Ratio Index	$RGRI = \frac{r}{g}$	(Albetis et al. 2017, Albetis et al. 2019, Cai et al. 2018)	
	Green Blue Ratio Index	$GBRI = \frac{b}{g}$	(Vilela et al. 2024)	
	Triangular Greenness Index	$TGI = g - 0.39 * r - 0.61 * b$	(Garza et al. 2020)	
	Greenness Index	$GI = \frac{g}{r}$	(Sanseechan et al. 2019)	
	Multispectral	Normalized Difference Vegetation Index	$NDVI = \frac{NIR - R}{NIR + R}$	(Guo et al. 2021, Wu et al. 2023)
		Red Edge Normalized Difference Vegetation Index	$NDRE = \frac{NIR - RE}{NIR + RE}$	(Chang et al. 2020, Albetis et al. 2019, Wu et al. 2023)
		Green Normalized Difference Vegetation Index	$GNDVI = \frac{NIR - G}{NIR + G}$	(Sanseechan et al. 2019)
		Green Chlorophyll Index	$Clg = \frac{NIR}{G} - 1$	(Ye et al. 2020)
Red Edge Chlorophyll Index		$Clre = \frac{NIR}{RE} - 1$	(Albetis et al. 2019, Ye et al. 2020)	
Chlorophyll Vegetation Index		$CVI = \frac{NIR}{G} * \frac{R}{G}$	(Wu et al. 2023)	
Difference Vegetation Index		$DVI = NIR - R$	(Steddom et al. 2005, Jie et al. 2015)	
Red Edge Green Index		$REGI = \frac{RE - G}{RE + G}$	(Albetis et al. 2019)	
Anthocyanin Reflectance Index		$ARI = \frac{1}{G} - \frac{1}{RE}$	(Ashourloo et al. 2014, Abdulridha et al. 2019)	
Plant Senescence reflectance Index		$PSRI = \frac{R - G}{NIR}$	(Ashourloo et al. 2014, Guo et al. 2021, Wu et al. 2023)	

verified by visually inspecting residual distribution plots and performing Levene's test, respectively. If these assumptions were violated (non-normal residuals or unequal variances), the non-parametric Kruskal-Wallis test was applied instead. When significant differences were detected, post-hoc tests were applied to determine pairwise differences between vitality classes. For ANOVA, pairwise t-tests with Holm's correction were conducted. For Kruskal-Wallis, pairwise Wilcoxon rank-sum tests with Bonferroni correction were used. This approach enabled the identification of vegetation indices suitable for assessing ash dieback damage.

To establish a threshold separating the value range of a vegetation index for mild and severe damage the datasets of both seed orchards were merged to generate universal thresholds. Extreme outlier values were adjusted by limiting all values higher than the 95th percentile to the 95th percentile value, and all values lower than the 5th percentile to the 5th percentile value. Vegetation indices were then normalized using Eq. 4, scaling all indices to a range of 0–1. To simplify the vitality data, classes 1 and 2 were combined to represent mild damage, while classes 3

and 4 were combined to represent severe damage. Due to the extended spread of ash dieback in Germany (Fuchs et al., 2024), no healthy trees (class 0) were found on the two study sites. Since the focus of our study lies on the analysis of leaf mass, dead trees (class 5) were excluded from the analysis. To determine whether the index values significantly differentiate between mild and severe damage for the three best RGB and multispectral indices, we assessed the normality of the data distribution using the Shapiro-Wilk test. As for none of the indices the assumption of normality was met, the Mann-Whitney *U* test was applied.

$$VI_{normalized} = \frac{VI - VI_{min}}{VI_{max} - VI_{min}} \quad (4)$$

A density plot was generated for each vegetation index in each UAV survey to display the index value range for the two damage classes, mild and severe. The intersection point of these distributions was identified as the optimal threshold for distinguishing between the two damage classes. Since each vegetation index was calculated for every UAV survey, an average threshold value was then determined across all surveys. This established average threshold was then re-evaluated across all surveys. Each threshold was verified by 10-fold cross-validation, where the original datasets were resampled into 10 sub-datasets. Overall accuracy (OA) (Eq. 6) and F1 score (Eqs. 6–8) were calculated to assess threshold performance. True positives (TP) and true negatives (TN) represented correct predictions that aligned with actual observations, while false positives (FP) and false negatives (FN) indicated incorrect predictions. OA represents the percentage of correct predictions. Precision measures the accuracy of positive predictions, while recall evaluates the ability to identify all relevant positive instances. As a measure of the optimal balance between precision and recall, the F1 score highlights the correctly identified TP and TN (Fawcett, 2006).

$$OA = \frac{TP + TN}{TP + FP + FN + TN} \quad (5)$$

$$Precision = \frac{TP}{TP + FP} \quad (6)$$

$$Recall = \frac{TP}{TP + FN} \quad (7)$$

$$F1Score = 2 * \frac{Precision * Recall}{Precision + Recall} \quad (8)$$

Additionally, due to the imbalance between the number of cases in the classes mild and severe, i.e., a higher prevalence of mildly damaged trees, the Matthews Correlation Coefficient (MCC; Eq. 9), was calculated. The MCC considers the balance of TP, TN, FP, and FN, offering a robust and unbiased evaluation metric, particularly in scenarios with class imbalance. MCC values can range from –1–1, with higher values indicating better model performance (Chicco and Jurman, 2020, Foody, 2023).

$$MCC = \frac{TP * TN - FP * FN}{\sqrt{(TP + FP) * (TP + FN) * (TN + FP) * (TN + FN)}} \quad (9)$$

All analyses were performed in R (version 4.1.1) using R Studio (version 2021.09.0).

**2.2.2.4. Combination of indices.** To improve damage estimation, we tested combinations of multiple VIs using binary logistic regression with 10-fold cross-validation. This method allows us to predict whether an outcome will be present or absent based on several predictor variables. The dependent variable is either 0 (mild damage) or 1 (severe damage). The model estimates the influence of each independent variable, in this case the various VIs, on the outcome, the disease severity. The dependent variable (*P*), the probability of the disease severity, was calculated according to Eq. 10 (Lee and Pradhan, 2007, Ye et al., 2020).

$$P = \frac{1}{1 + e^{-y}} \quad (10)$$

The variable  $y$  is a linear combination calculated according to Eq. 11 (Lee and Pradhan, 2007, Ye et al., 2020)

$$y = b_0 + b_1x_1 + b_2x_2 + b_3x_3 + b_nx_n \quad (11)$$

Here,  $b_0$  is the intercept,  $b_1$  are the slope coefficients, and  $x_1$  represent the independent variables. In this study, this equation was applied to model the probability of the disease severity based on the thresholds of multiple, combined VIs. The `glm()` function of the R package “car” was utilized to fit the logistic regression models.

For both RGB and multispectral data, the three indices, which were most successful in discriminating the damage severity with thresholding were selected and combined in the logistic regression model to determine the efficiency of the calculated thresholds in combination with other indices.

A correlation analysis was conducted between these six indices to assess their relationships. To avoid multicollinearity, which can lead to unstable regression models, only indices with a low correlation were selected from both the RGB and multispectral data. Multicollinearity was tested for applying variance inflation factor (VIF) analysis, using the function `vif()` in the “car” package in R. The smallest VIF value is 1, values greater than 5 indicate multicollinearity. VIF was calculated using Eq. 12 where  $R^2$  represents the coefficient of determination, which measures how well one independent variable can be predicted by all the other independent variables in the model. If the  $R^2$  value is close to 1, the variable is highly related to the others (collinearity), resulting in a high VIF. In such cases, the variable does not provide much unique information to the model (James et al., 2023).

$$VIF = \frac{1}{1 - R^2} \quad (12)$$

Binary logistic regression analysis was used to determine whether combining RGB and multispectral data improves the accuracy of damage severity estimation.

The results of the logistic regression analysis were again assessed with a 10-fold cross-validation, focusing on the statistical measures of OA, F1 score and MCC.

**2.2.2.5. Processing of the thermal images.** Since the thermal images captured by the Mavic 2 EA were initially saved as 8-bit JPEG-files, a pre-processing of the images was necessary, converting them into 16-bit TIFF-files. An adapted R script, based on the script developed by Kattenborn (2023), was used for facilitating this image conversion. This ensured a consistent scale across all images, where each specific temperature value corresponded to the same digital number, enabling the application of structure-from-motion processing. The script is based on the DJI Thermal SDK (version 1.4) and incorporated factors such as emissivity, relative humidity, and camera-target-distance.

Relative humidity was measured on both study sites using a relative humidity logger (HOBO U23-001, Onset, Bourne, MA, USA) recording data every ten minutes. We used the mean relative humidity during the flight time and an emissivity value of 0.96 was applied for all images, based on the estimated average emissivity value for plants determined by Harrap et al. (2018).

The converted thermal images were validated randomly using the DJI Thermal Analysis Tool (version 2.1.8). Afterwards the converted images were stitched together to an orthomosaic as described for the RGB and multispectral images.

In the final thermal orthophoto, individual ash tree crowns were segmented manually in ArcGIS Pro. Using the tool “zonal statistics”, the mean temperature per segmented tree crown was calculated. To determine statistically significant differences in mean crown temperatures across vitality classes, we followed the statistical procedure described above (chapter 2.2.2.3).

### 3. Results

#### 3.1. Vegetation indices

##### 3.1.1. Multispectral indices

The comparison of mean values related to the VIs and the respective vitality classes revealed varying outcomes depending on the specific VI and the seasonal timing of the UAV surveys. For all indices, severe damage was associated by decreased index values. At the Emmendingen seed orchard, all ten VIs were able to significantly discriminate between the four vitality classes in the summer, with  $p$  values  $< 0.001$  for both surveys in June and July (Table 3). At the Schorndorf seed orchard, all indices except the CVI showed significant differentiation in June, only six out of ten indices were significant in July. The VIs generated from the autumn surveys performed worse than those from the summer. Only seven VIs for Emmendingen and five for Schorndorf showed statistically significant differences between the classes. Overall, the multispectral VIs NDVI, GNDVI, Clg, REGI and DVI were able to discriminate between the vitality classes for all surveys in both summer and autumn. The post-hoc tests revealed that the majority of indices presented significant differences between class 1 and 3 and class 1 and 4, whereas typically only a few significant differences between class 1 and 2 and class 3 and 4 could be detected. Due to the extensive size of the post-hoc results, they are not presented here.

For each VI, mean thresholds were calculated across all surveys to distinguish between mild damage (vitality classes 1 and 2) and severe damage (vitality classes 3 and 4). For example, NDVI values above the calculated summer threshold of 0.57 were classified as mildly damaged, whereas NDVI values below this threshold represented severely damaged ash trees. Validation of these mean thresholds applying 10-fold cross-validation revealed varying classification success rates (Table 4). Among the thresholds derived from both summer and autumn surveys, the DVI and GNDVI achieved the highest accuracy and F1 scores, with classification success rates of 71.4 % and 71.5 %, respectively. When considering only the summer surveys, the highest classification success was again observed for DVI and GNDVI, with an OA of 74.9 % and 74.4 %, respectively. Although the REGI ranked third for both summer and autumn data with an accuracy of 70.8 %, the NDVI demonstrated a higher OA of 73.9 % when evaluated solely with summer data. Especially for the summer surveys, the combination of a relatively high OA, a high F1 score, and a moderate MCC suggests that the thresholds perform reasonably well overall. Due to the class imbalance, the overall accuracy (OA) is influenced by the larger class of mildly damaged trees. The high F1 score suggests balanced classification performance across both damage classes. Additionally, the MCC exceeds 0.4, indicating moderate agreement beyond chance, quantifying the effectiveness of the thresholds in distinguishing between mildly and severely damaged trees.

Boxplots illustrating vegetation indices (NDVI, DVI, and GNDVI) from all four summer surveys conducted at the Emmendingen and

**Table 3**

P-values for the statistical difference between the four vitality classes for the ten selected multispectral VIs at the Emmendingen (E) and Schorndorf (S) seed orchards in 2023; Definition of VIs see Table 2. Bold values: significant at the 5 % level.

	E June 23	E July 23	E Oct 23	S June 23	S July 23	S Oct 23
NDVI	<b>&lt; 0.001</b>	<b>0.006</b>				
NDRE	<b>&lt; 0.001</b>	<b>&lt; 0.001</b>	<b>0.009</b>	<b>&lt; 0.001</b>	0.057	0.068
GNDVI	<b>&lt; 0.001</b>	<b>&lt; 0.001</b>	<b>0.010</b>	<b>&lt; 0.001</b>	<b>0.001</b>	<b>0.019</b>
Clg	<b>&lt; 0.001</b>	<b>&lt; 0.001</b>	<b>0.019</b>	<b>&lt; 0.001</b>	<b>0.001</b>	<b>0.019</b>
Clre	<b>&lt; 0.001</b>	<b>&lt; 0.001</b>	<b>0.009</b>	<b>&lt; 0.001</b>	0.052	0.070
CVI	<b>&lt; 0.001</b>	<b>&lt; 0.001</b>	0.092	0.181	0.968	0.915
REGI	<b>&lt; 0.001</b>	<b>&lt; 0.001</b>	<b>0.015</b>	<b>&lt; 0.001</b>	<b>&lt; 0.001</b>	<b>0.018</b>
PSRI	<b>&lt; 0.001</b>	<b>&lt; 0.001</b>	0.148	<b>&lt; 0.001</b>	0.757	0.819
DVI	<b>&lt; 0.001</b>	<b>0.001</b>				
ARI	<b>&lt; 0.001</b>	<b>&lt; 0.001</b>	0.068	<b>&lt; 0.001</b>	0.220	0.396

**Table 4**

Established thresholds, overall accuracy (OA), F1 score (F1) and Matthews correlation coefficient (MCC) for the ten selected multispectral VIs, considering combined summer and autumn surveys as well as summer surveys only.

	Summer and autumn surveys				Summer surveys			
	Threshold	OA	F1	MCC	Threshold	OA	F1	MCC
NDVI	0.58	70.2	0.76	0.38	0.57	73.9	0.80	0.44
DVI	0.50	71.4	0.78	0.38	0.52	74.9	0.80	0.46
NDRE	0.48	64.3	0.70	0.29	0.45	68.8	0.75	0.35
Clg	0.36	70.5	0.77	0.37	0.38	72.1	0.79	0.38
Clre	0.46	63.5	0.69	0.28	0.43	68.3	0.74	0.34
GNDVI	0.44	71.5	0.78	0.37	0.46	74.5	0.81	0.43
CVI	0.29	63.4	0.72	0.17	0.31	66.7	0.75	0.26
REGI	0.45	70.8	0.78	0.36	0.47	72.4	0.79	0.38
ARI	0.33	66.3	0.74	0.26	0.37	68.3	0.75	0.32
PSRI	0.50	30.6	0.67	0.21	0.49	63.4	0.71	0.22

Schorndorf seed orchards (Fig. 3) show a clear significant difference in median positions (solid horizontal lines within the boxes), indicating distinct vegetation responses between mildly and severely affected ashes. However, varying degrees of overlap in the interquartile ranges (box height) were evident among indices. The dashed line in Fig. 3 represents the calculated threshold separating mildly and severely damaged trees.

### 3.1.2. RGB indices

The ten selected RGB indices exhibited varying degrees of suitability for differentiating among the vitality classes. For the RGRI and the ExR indices, severe damage is indicated by higher values, while for all other RGB indices, more severe damage is linked to decreased index values. While some indices demonstrated statistically significant differences among the four vitality classes, only the GLI index proved significance across all surveys conducted from May to October at both study sites (Table 5). The ExG and RGBVI indices also widely displayed statistically significant differences in vitality classes for most surveys, except for the May 2022 survey in Emmendingen. Although the GRVI and GI indices were not significantly different during the autumn 2022 surveys, they achieved statistical significance in October 2023. The autumn surveys for both years indicated a reduced ability of RGB VIs to distinguish between vitality classes. However, in Schorndorf in 2023, most indices achieved statistical significance. As for the multispectral indices, the post-hoc tests (not shown) demonstrated mostly significant differences between class 1 and 3 and class 1 and 4, and only in some cases significant differences between class 1 and 2 and class 3 and 4. Post-hoc test results supported the classification of classes 1 and 2 as mild damage and classes 3 and 4 as severe damage, making this grouping suitable for further threshold analysis.

Thresholds generated for the RGB-derived VIs varied between the combined summer and autumn surveys and the summer-only surveys. Validation through 10-fold cross-validation indicated that the ExG, GLI,

and RGRI indices achieved the highest accuracy and F1 scores for the combined summer/autumn surveys, with ExG attaining the highest accuracy at 71.0 %. In contrast, slightly higher accuracies were recorded for the summer-only surveys, where the GRVI, ExG, and RGRI were most effective in distinguishing between mild and severe damage due to ash dieback. The highest OAs were observed during the summer surveys, with the GRVI achieving 73.0 %, followed by the RGRI at 72.5 % and the ExG at 72.2 %. As with the multispectral indices, a relatively high OA was generally associated with a high F1 score and a moderate MCC for the three most successful indices. However, for the RGB indices, the MCC values only exceeded the threshold for moderate agreement of 0.4 for the GRVI in the summer; all other indices presented lower MCC values (Table 6).

Although a clear statistically significant shift in the median is visible (Fig. 4), the determined thresholds (dashed lines) cannot entirely separate the two damage classes due to overlapping interquartile ranges. For GRVI and ExG, more severe damage leads to decreased index values, whereas for RGRI, higher values indicated severe damage.

### 3.1.3. Combination of indices

The results of the binary logistic regression analysis for three combinations of VIs are presented in Table 7. All three combinations, which include the most appropriate VIs for thresholding, yielded very similar outcomes, with accuracies ranging from 76.7 % to 77.2 %, F1 scores between 0.83 and 0.84, and the MCC between 0.43 and 0.48. The highest classification success was achieved using the combination of two multispectral indices (NDVI and DVI) and one RGB index (ExG), which also exhibited low VIF values. This combination is the only pairing of RGB and multispectral indices with low VIF values; all other combinations exhibited multicollinearity. For instance, the combination of the three RGB indices – GRVI, ExG, and REGI – also showed high VIF values exceeding the threshold of 10 for both GRVI and RGRI, indicating multicollinearity. Conversely, both the multispectral index combination

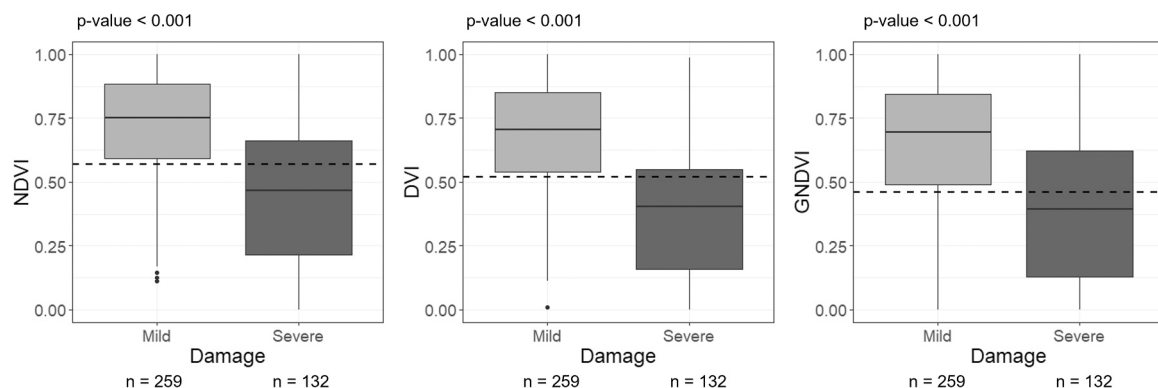


**Fig. 3.** Boxplots of all four summer surveys for the merged dataset of the Emmendingen and Schorndorf seed orchards, displaying the normalized vegetation indices NDVI, DVI and GNDVI for the trees.

**Table 5**

P-values for the statistical differences between the four vitality classes for the ten selected RGB VIs at the Emmendingen (E) and Schorndorf (S) seed orchards in 2022 and 2023. Bold values: significant at the 5 % level.

	E May 22	E July 22	E Okt. 22	S June 22	S Okt. 22	E June 23	E July 23	E Okt. 23	S June 23	S July 23	S Okt. 23
GRVI	< 0.001	< 0.001	0.080	< 0.001	0.975	< 0.001	< 0.001	< 0.001	< 0.001	< 0.001	<b>0.005</b>
ExG	0.099	< 0.001	<b>0.001</b>	< 0.001	<b>0.006</b>	< 0.001	< 0.001	< 0.001	< 0.001	< 0.001	< 0.001
ExR	0.052	< 0.001	0.251	0.444	< 0.001	< 0.001	< 0.001	<b>0.016</b>	<b>0.009</b>	0.053	0.088
ExGR	<b>0.004</b>	< 0.001	0.379	0.092	0.060	< 0.001	< 0.001	<b>0.002</b>	< 0.001	<b>0.001</b>	<b>0.035</b>
GLI	<b>0.034</b>	< 0.001	<b>0.001</b>	< 0.001	<b>0.006</b>	< 0.001	< 0.001	< 0.001	< 0.001	< 0.001	< 0.001
RGBVI	0.130	<b>0.012</b>	< 0.001	< 0.001	<b>0.001</b>	<b>0.010</b>	<b>0.037</b>	<b>0.003</b>	< 0.001	< 0.001	< 0.001
GI	< 0.001	< 0.001	0.080	< 0.001	0.978	< 0.001	< 0.001	< 0.001	< 0.001	< 0.001	<b>0.003</b>
RGRI	< 0.001	< 0.001	0.073	< 0.001	0.976	< 0.001	< 0.001	< 0.001	< 0.001	< 0.001	<b>0.005</b>
GBRI	0.568	0.258	<b>0.003</b>	< 0.001	< 0.001	0.751	0.362	<b>0.04</b>	< 0.001	< 0.001	< 0.001
TGI	0.199	0.026	<b>0.002</b>	< 0.001	< 0.001	<b>0.034</b>	0.017	< 0.001	< 0.001	< 0.001	< 0.001

**Table 6**

Established thresholds, overall accuracy (OA), F1 score (F1) and Matthews correlation coefficient (MCC) for the ten selected RGB VIs for the combined summer and autumn surveys and the summer-only surveys.

	Summer and autumn surveys				Summer surveys			
	Threshold	OA	F1	MCC	Threshold	OA	F1	MCC
GRVI	0.42	67.3	0.74	0.34	0.37	73.0	0.80	0.40
ExG	0.45	71.0	0.78	0.36	0.42	72.2	0.80	0.35
ExR	0.61	60.3	0.68	0.18	0.58	63.0	0.69	0.27
ExGR	0.37	63.6	0.71	0.24	0.38	67.6	0.74	0.34
GLI	0.48	70.2	0.77	0.35	0.45	71.5	0.79	0.35
RGBVI	0.48	68.0	0.76	0.29	0.47	67.5	0.75	0.27
RGRI	0.60	69.3	0.76	0.33	0.60	72.5	0.79	0.39
GBRI	0.48	63.2	0.71	0.21	0.47	60.8	0.69	0.18
TGI	0.47	66.5	0.74	0.27	0.46	65.7	0.74	0.25
GI	0.37	65.9	0.72	0.34	0.32	70.8	0.77	0.38

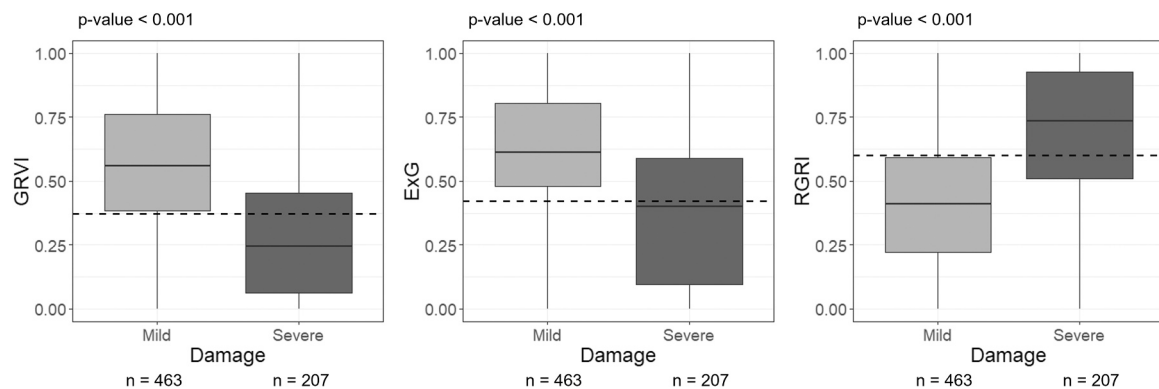


**Fig. 4.** Boxplots of all seven summer surveys for the merged data of the Emmendingen and Schorndorf seed orchards, displaying the vegetation indices GRVI, ExG and RGRI for the trees surveyed in the summer.

and the combined RGB and multispectral indices displayed low VIF values, suggesting the absence of multicollinearity.

The correlations among the six selected VIs (Fig. 5) partially revealed strong relationships not only within the RGB and multispectral datasets but also across them. These high correlations limited the improvement in damage severity identification, resulting in a 2 % higher OA compared to using individual indices alone.

### 3.2. Thermal images

The analysis of the thermal images in relation to the different vitality classes revealed different distributions of crown temperatures for the four vitality classes. Statistically significant differences were recorded in only two of the ten UAV surveys (Fig. 6). Specifically, in June ( $p < 0.001$ ) and in October ( $p = 0.021$ ) 2023 at the Schorndorf seed orchard, a significant increase in crown temperature was observed in more severely affected ash trees. The post-hoc test for the June survey

revealed significant differences between class 1 and class 4 ( $p = 0.006$ ), class 2 and class 4 ( $p < 0.001$ ), and class 3 and class 4 ( $p = 0.025$ ). In the October survey, a statistically significant difference was observed only between class 1 and class 4 ( $p = 0.031$ ). Although a similar trend was visually apparent in some other UAV surveys, it did not reach statistical significance in those cases. An exception was the May 2022 survey in Emmendingen, which exhibited an opposing pattern with a temperature decrease of over 2 °C between the medians of vitality classes 1–4.

## 4. Discussion

In this study, three different camera systems - RGB, thermal and multispectral - were tested for their suitability to differentiate between varying degrees of damage caused by ash dieback.

Due to the rapid progression of ash dieback, no healthy tree could be included in this study. Consequently, the analysis focused solely on trees exhibiting varying degrees of damage. However, it is important to note

**Table 7**

Logistic regression equations for three different combinations of indices with their overall accuracy (OA), F1 score (F1), Matthews correlation coefficient (MCC) and the variance inflation factor (VIF).

Data	Logistic Regression Equation	OA	F1	MCC	VIF
MS	$y = 0.9294608 - 0.3666048 \text{ NDVI} - 1.386887 \text{ DVI} - 1.005055 \text{ GNDVI}$	76.7 %	0.83	0.46	NDVI: 2.4 DVI: 1.5 GNDVI: 1.9
RGB	$y = 0.5276535 - 0.7400043 \text{ GRVI} - 0.869358 \text{ ExG} - 0.6269988 \text{ RGRI}$	76.9 %	0.84	0.43	GRVI: 14.2 ExG: 1.3 RGRI: 13.8
MS and RGB	$y = 1.024588 - 0.613737 \text{ NDVI} - 1.44662 \text{ DVI} - 0.8624887 \text{ ExG}$	77.2 %	0.83	0.48	NDVI: 1.8 DVI: 1.5 ExG: 1.3

that only a few severely damaged trees (class 4) existed on both study sites. We propose that classification performance could improve at sites with a higher prevalence of both healthy and severely damaged trees. This is because the contrast in spectral reflectance properties between the healthiest and most damaged trees is likely to provide clearer distinctions for analysis. Therefore, we suggest that further studies should especially focus on trees in class 4 and, if possible, also in class 0.

**4.1. RGB and multispectral UAV data**

Clear results could be obtained using RGB data for differentiation between mild and severe damage due to ash dieback. As outlined below,

numerous studies have demonstrated similar results, emphasising the usability of RGB data in the context of plant diseases especially in agricultural crops. A significant relationship between RGB indices and winter wheat foliage disease severity has been proven using a low-cost UAV equipped with a digital camera (Bhandari et al., 2020). RGB images focusing on citrus trees (*Citrus* spp.) affected by diseases were able to demonstrate lower triangular greenness index (TGI) values for diseased trees (Garza et al., 2020). For the detection of narrow brown leaf spot severity in rice (*Oryza* spp.), the ExGR index was the most suitable for detecting high levels of disease (Cai et al., 2018). Various indices were tested for each case study and the success of each VI to differentiate between the damage severity varied greatly. In this study, the GRVI, ExG and RGRI were found to be capable of differentiating between mild and severe damage with the applied threshold with the highest accuracies. RGB VIs can amplify subtle differences in vegetation health that may not be visually discernible in raw RGB images, making them a valuable tool for in-depth plant health analysis by providing quantifiable and standardized metrics of vegetation condition.

The generated multispectral data in combination with various VIs and associated thresholds were also successfully applied to differentiate between mild and severe damage. Numerous studies utilized multi-spectral indices to identify disease occurrence or severity in plants. For citrus trees (*Citrus* spp.), infected by Citrus greening disease, four VIs demonstrated significant higher index values in healthy than in diseased trees (Chang et al., 2020). Multispectral indices were also suitable for the differentiation between healthy banana plants (*Musa* spp.) and plants affected by banana Fusarium wilt disease (Ye et al., 2020). The detection of canker infected citrus trees (*Citrus* spp.) was possible utilizing multispectral VIs (Abdulridha et al., 2019). Although in our study all multispectral indices were able to distinguish between mild and

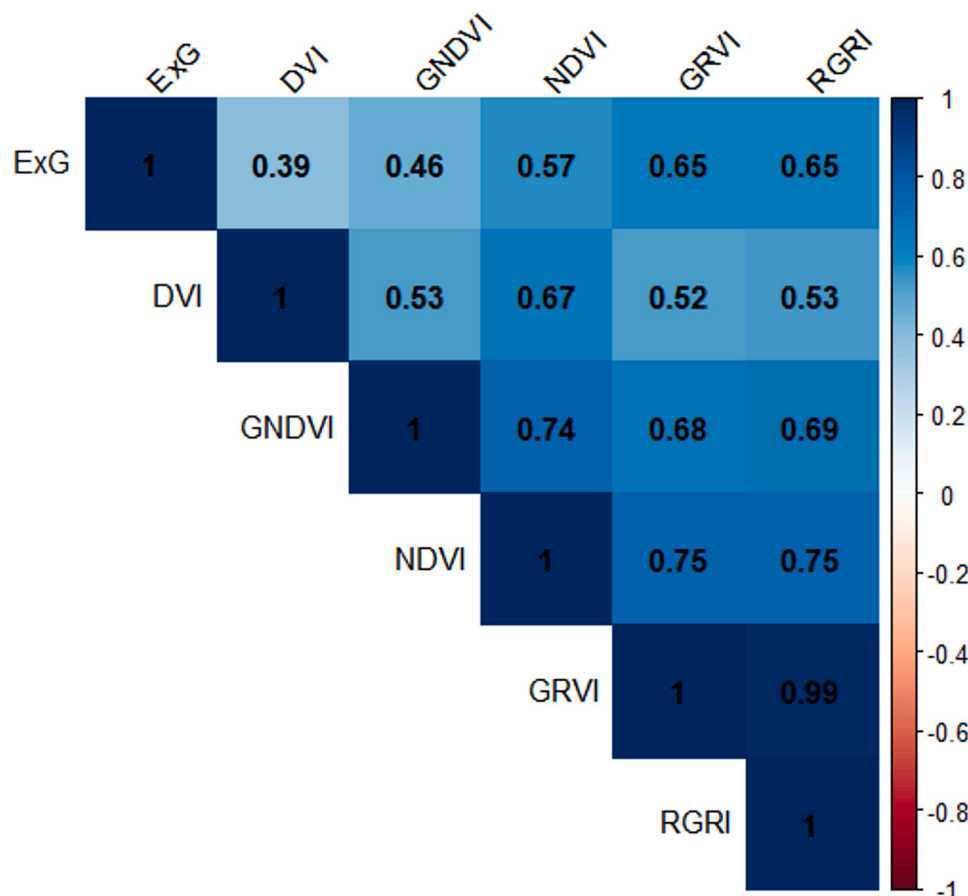


**Fig. 5.** Correlations between the three selected RGB and multispectral indices: ExG, DVI, GNDVI, NDVI, GRVI and RGRI.

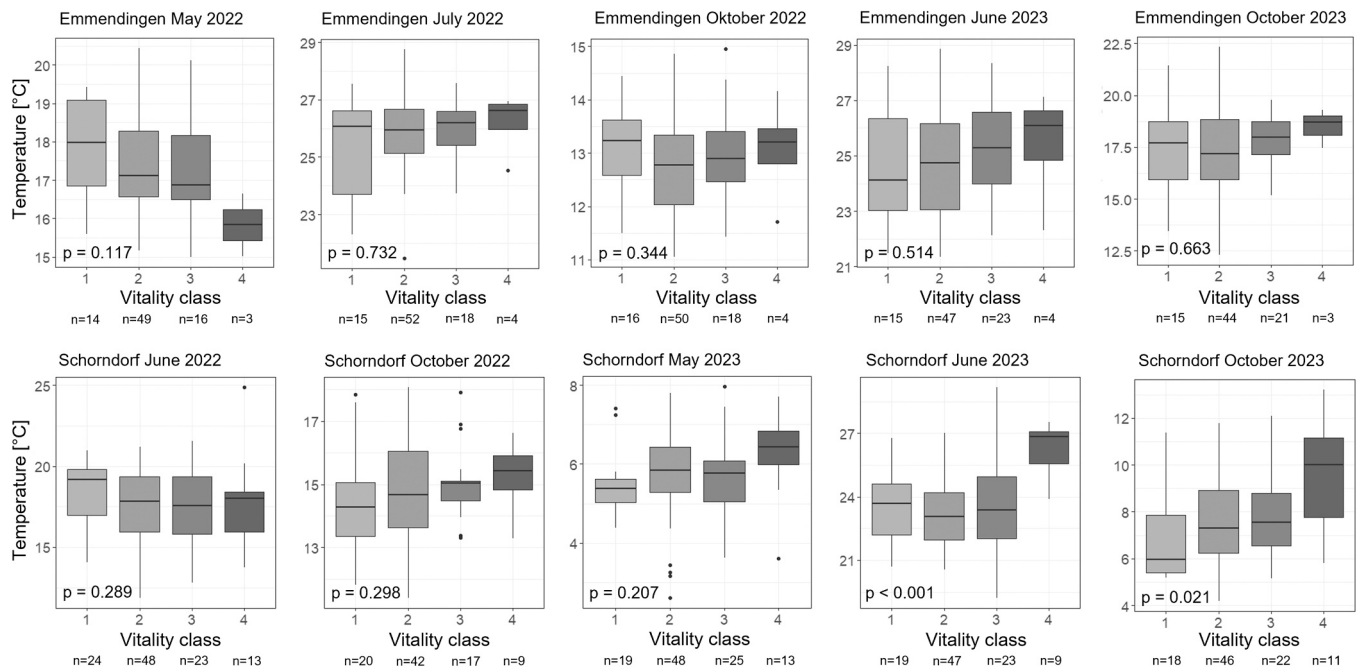


Fig. 6. Boxplots of the crown temperature of the ash trees for the different vitality classes for 2022 and 2023 for both study sites.

severe damage, the highest accuracies were achieved for the GNDVI, NDVI and DVI. While red-edge indices are often highlighted as being effective in identifying diseased plants (Chang et al., 2020, Ye et al., 2020), we found that they did not outperform indices without the red-edge band. Instead, the red, green, and NIR bands were particularly successful in determining the severity of damage caused by ash dieback.

Autumn UAV surveys for both RGB and multispectral data performed worse compared to those conducted in the summer. Overall, the autumn indices showed fewer significant differences between the four vitality classes than the indices calculated from the summer surveys. When factored into the calculated mean threshold, the accuracy of classifying the two damage classes was lower than during the summer months only, indicating reduced effectiveness. Since the autumn surveys were conducted in October, early stages of leaf senescence had likely begun, influencing the spectral reflectance of the leaves and reducing the observable effects of ash dieback. Despite this, VIs from October surveys effectively distinguished between mild and severe damage, confirming that UAV-based assessments are possible throughout the entire vegetation period of the common ash. However, thresholds solely from summer surveys were more reliable, making summer the recommended period for more accurate and stable assessments.

#### 4.2. Thermal UAV data

The use of a thermal UAV camera in our study proved less effective than the RGB and multispectral data in distinguishing crown temperatures of ash trees in relation to disease severity. While an expected increase in crown temperature with more advanced symptoms of ash dieback was observed in seven out of ten conducted surveys, the difference between the damage classes were only seldom statistically significant. In contrast, numerous studies, focusing on agricultural crops, have demonstrated clearer results when applying thermal cameras for plant disease detection. For tomato (*Solanum* spp.) plants infected with *O. neolyopersici*, thermal images provided information in regards to the identification of diseased plants (Raza et al., 2015). Rose plants (*Rosa hybrida* L.), affected by powdery mildew (*Podosphaera pannosa* var. *rosae*) and gray mold (*Botrytis cinerea*) also presented clear changes in their thermal appearance (Jafari et al., 2017). With an accuracy of over 90 %, disease-induced spots in banana (*Musa* spp.) leaves were able to

be identified using a thermal camera (Anasta et al., 2021). A significant leaf surface temperature increase was observed for avocado (*Persea americana* Mill.) plants infected with white root rot (Granum et al., 2015) as well as sunflower (*Helianthus annuus* L.) plants infected with *Orobancha cumana* (Ortiz-Bustos et al., 2017). However, these studies primarily focused on ground-based thermal images of individual leaves or smaller plants, allowing for precise identification of affected areas. In contrast, our study employed UAV-based thermal imaging at a flight height of 80 m above the ground, with an image resolution of 10.48 cm/pixel. This approach may have limited the ability to detect small areas of increased temperature associated with ash dieback and might not be represented proportionately in the final orthophoto. The mean temperature per tree crown calculated in this study could therefore underrepresent leaf areas with increased temperature due to an infection with ash dieback and the associated presumed stress-induced closure of stomata.

For detecting *Xylella fastidiosa* infections in olive (*Olea europaea*) orchards using remote sensing techniques, the integration of thermal imaging with multispectral data significantly enhanced identification accuracy, highlighting the potential of thermal remote sensing data to detect plant diseases (Poblete et al., 2020). Smigaj et al. (2015) proved that UAV-borne thermal image data can detect temperature differences linked to red band needle blight (*Dothistroma septosporum*) infection status at the tree level for pine trees (*Pinus sylvestris* and *Pinus contorta*) in a forest. Studies investigating leaf temperature changes in disease-inoculated plants have documented an initial temperature decrease before visible symptoms emerge, followed by a subsequent increase as the disease progresses. The pre-symptomatic temperature reduction is linked to stomatal opening, while the later rise above healthy tissue levels is associated with chlorosis and cell death (Lindenthal et al., 2005, Baranowski et al., 2015, Jafari et al., 2017). Therefore, contradicting results as found in our study, might hinder a clear interpretation of thermal images. In our approach, the mean crown temperature includes all leaves within a tree crown, meaning that variations in thermal dynamics due to differing infection statuses among the leaves cannot be ruled out and may counterbalance each other. The thermal sensor of the Mavic 2 EA has been proven to record temperatures with a deviation of up to 2 °C compared to ground-based temperature measurements (Leblanc et al., 2021). Additionally, factors such

as wind direction and flight speed can influence the accuracy of thermal imaging (Malbéteau et al., 2021). Although the captured thermal images were calibrated in terms of emissivity, relative humidity and camera-target-distance, inaccuracies related to the actual crown temperatures cannot be entirely excluded. Further studies would benefit from the inclusion of more severely damaged trees as these trees were underrepresented at our study sites. We suggest that this group of trees can be best delineated from other vitality classes, as demonstrated by most surveys in Schorndorf. In Emmendingen, proper conclusions are especially lacking due to the low number of ashes in class 4 with very severe damage ( $n < 5$ ). Since the pattern observed in our study suggests that crown temperature differences exist, further investigations and a continuing monitoring of thermal characteristics in the context of ash dieback could be promising. UAV surveys with a lower flight height could improve the resolution of the images and are therefore recommended for further studies.

#### 4.3. Vegetation index thresholding

The use of fixed threshold, whether to distinguish healthy from diseased plants or to differentiate between varying degrees of damage, provides a clear and practical method for interpreting VIs. Various thresholding techniques in the context of VIs and remote sensing data have already been tested in prior studies (Suh et al., 2020). Albetis et al. (2017) identified optimal thresholds for various VIs to distinguish grapevines (*Vitis vinifera* L.) affected by *Flavescence dorée* disease from healthy, symptom-free individuals. However, the optimal thresholds varied among the different studied cultivars, limiting the reproducibility. Similarly, VI thresholds calculated for *Flavescence dorée* disease and Grapevine Trunk Disease demonstrated the challenge of correctly distinguishing between the two diseases and asymptomatic plants (Albetis et al., 2019).

In our study, a perfect separation of mild and severe damage due to ash dieback using a threshold was difficult to achieve. The highest accuracy of 74.9 % was obtained calculating the DVI threshold. However, the overlap between mild and severe damage classes likely reflects the “fluid” health status of the ash trees, which were categorized into fixed classes. The vitality assessments in the field relied on the observer’s judgment, and although all evaluations were performed by the same trained expert, minor discrepancies may have occurred. The distinction between class 2, representing mild damage, and class 3, representing severe damage, is often minimal, e.g., for the least healthy trees in class 2 and the healthiest trees in class 3. Since the use of a threshold is highly praxis-oriented, this study focused on a simple, manageable workflow for forest practitioners as an alternative to more complex classifying methods, an approach also emphasized by Otsu et al. (2019).

The correlation analysis of the three RGB and three multispectral indices indicated high correlations between all indices. As a result, combining multiple indices – whether RGB, multispectral, or a mix of both – did not substantially improve classification accuracy. The most promising combination in determining the severity of ash dieback damage, with an accuracy of 77.2 %, was achieved combining the two multispectral indices NDVI and DVI and the RGB index ExG. However, due to the limited number of datasets, the training datasets used to calculate the mean thresholds were resampled for validation, which may result in slightly higher accuracy scores, as noted by Yadav and Shukla (2016).

Few studies have aimed to classify ash dieback severity using remote sensing data, and achieving fully accurate classifications remains a challenge. Waser et al. (2014) used WorldView-2 satellite data with 19 VIs to classify four levels of ash health in a German forest site, achieving an overall accuracy of 77 %, which is similar to our classification results. An analysis using hyperspectral forest data, providing a broader range of wavelengths, likewise reached a 77 % accuracy in classifying damage severity within a Random Forest model (Chan et al., 2021). Polk et al. (2022) identified ash trees infected with *Hymenoscyphus fraxineus* at a

forest site without focusing on severity, achieving 71 % accuracy using hyperspectral data. In another study, Kampen et al. (2019) used UAV-based multispectral data and a Random Forest classifier to identify five levels of ash dieback severity at an ash seed orchard, achieving an accuracy of 61.7 %. The results of these studies highlight the difficulty of correctly separating ash dieback damage classes.

The differentiation of damage severity, however, can be achieved not only with hyper- or multispectral data. As our study revealed, a single RGB index, such as GRVI, can also be used to determine damage severity with an OA of 73 %. While ash seed orchards offer advantages in detecting individual ash trees, previous studies have shown that ash dieback severity analysis can also be achieved in forest sites (Waser et al., 2014, Chan et al., 2021, Polk et al., 2022).

Both RGB and multispectral data effectively assess ash dieback severity using VIs and thresholds, though thermal data was less effective. Multispectral data provided slightly higher classification accuracy, but RGB data also performed well. While both UAV systems are similar in cost and usability, multispectral cameras are generally more expensive and complex to operate.

Ash dieback presents an important threat to common ash trees across Europe, and largescale health assessments of affected trees have been highly time-consuming and labor-intensive. The use of fixed thresholds applied to orthophotos generated from UAV surveys offers new, practical opportunities for assessing the health status of *Fraxinus excelsior* L. This method offers a significant time advantage, particularly for large-scale assessments, while also enabling the monitoring of otherwise inaccessible areas. Beyond health monitoring, this approach also holds potential for large-scale phenotyping and other applications. For conservation purposes, identifying ash trees with only mild damage symptoms is particularly relevant, as some individuals exhibit greater resistance to ash dieback than others (McKinney et al., 2011). Our method allows for the detection of trees with mild damage and facilitates long-term monitoring of their health status, which is crucial for further investigation and conservation efforts. Although this study focuses on ash seed orchards with relatively high tree spacing, the outlined approach is also applicable to forest stands. However, before applying the established VI thresholds, it is essential to identify the individual ash trees, e.g. as demonstrated by Waser et al. (2014) and Chan et al. (2021). Since our determined thresholds are based on the normalized range of VIs, applying them requires following our proposed workflow.

Due to the fluid progression of the state of health, a 100 % accurate classification of the damage in accordance with the field assessment is likely very difficult to achieve, however an estimation of the health status based on VIs is possible. The application of thresholds can enable targeted forestry care efforts to conserve this endangered tree species. Given current recommendation to preserve mildly affected ash trees rather than remove them (FNR, 2024), identifying trees with mild damage is highly relevant. With the ongoing progression of ash dieback, accurately identifying mildly damaged ash trees will become increasingly important for the long-term conservation of *Fraxinus excelsior* L.

## 5. Conclusion

UAV images are an important tool to investigate large areas of ash trees affected by ash dieback in a short time. Our study determined that UAV images captured during the summer months yield the most consistent results, offering comparable VI thresholds. Both RGB and multispectral data successfully enabled the generation of multiple VIs capable of identifying damage severity due to ash dieback. The thresholds derived in this study represent an important advancement for assessing extensive areas of affected ash trees, with single indices achieving classification accuracies of up to 74.9 % for estimating disease severity. The straightforward workflow, along with the specified thresholds for various indices, offers forest practitioners an important tool for identifying and managing ash dieback damage. However, given that our datasets were spatially, and temporally limited, further research

focused on refining these thresholds and enhancing classification accuracy is recommended.

## Funding

This study was conducted within the project FraxVir “Detection, characterisation and analyses of the occurrence of viruses and ash dieback in special stands of *Fraxinus excelsior* – a supplementary study to the FraxForFuture demonstration project” and receives funding via the Waldklimafonds (WKF) funded by the German Federal Ministry of Food and Agriculture (BMEL) and Federal Ministry for the Environment, Nature Conservation, Nuclear Safety and Consumer Protection (BMUV) administrated by the Agency for Renewable Resources (FNR) under grant agreement 2220WK40A4.

## CRediT authorship contribution statement

**Lisa Buchner:** Writing – original draft, Methodology, Investigation, Formal analysis. **Anna-Katharina Eisen:** Writing – review & editing, Methodology. **Susanne Jochner-Oette:** Writing – review & editing, Supervision, Funding acquisition, Conceptualization.

## Declaration of Generative AI and AI-assisted technologies in the writing process

During the preparation of this work the authors used ChatGPT in order to improve readability and grammar of a few sentences. After using this tool, the authors reviewed and edited the content as needed and take full responsibility for the content of the published article.

## Declaration of Competing Interest

The authors declare that they have no known competing financial interests or personal relationships that could have appeared to influence the work reported in this paper.

## Acknowledgements

We thank the Forestry Baden-Wuerttemberg and the Forest Research Institute Baden-Wuerttemberg for providing the seed orchards as study sites. We thank Tobias Heckmann and Manuel Stark for insightful discussions and support. Special thanks to all student assistants and Kathrin and Marlene Buchner for their technical assistance.

## Data availability

Data will be made available on request.

## References

- Abd El-Ghany, N.M., Abd El-Aziz, S.E., Marei, S.S., 2020. A review: application of remote sensing as a promising strategy for insect pests and diseases management. *Environ. Sci. Pollut. Res. Int.* 27 (27), 33503–33515. <https://doi.org/10.1007/s11356-020-09517-2>.
- Abdulridha, J., Batuman, O., Ampatzidis, Y., 2019. UAV-based remote sensing technique to detect citrus canker disease utilizing hyperspectral imaging and machine learning. *Remote Sens.* 11 (11), 1373. <https://doi.org/10.3390/rs11111373>.
- Albetis, J., Duthoit, S., Guttler, F., Jacquin, A., Goulard, M., Poilvé, H., Féret, J.-B., Dedieu, G., 2017. Detection of *Flavescence dorée* grapevine disease using Unmanned aerial vehicle (UAV) multispectral imagery. *Remote Sens.* 9 (4), 308. <https://doi.org/10.3390/rs9040308>.
- Albetis, J., Jacquin, A., Goulard, M., Poilvé, H., Rousseau, J., Clenet, H., Dedieu, G., Duthoit, S., 2019. On the potentiality of UAV multispectral imagery to detect *Flavescence dorée* and grapevine trunk diseases. *Remote Sens.* 11 (1), 23. <https://doi.org/10.3390/rs11010023>.
- Anasta, N., Setyawan, F.X.A., Fitriawan, H., 2021. Disease detection in banana trees using an image processing-based thermal camera. *IOP Conf. Ser. Earth Environ. Sci.* 739 (1), 12088. <https://doi.org/10.1088/1755-1315/739/1/012088>.
- Ashourloo, D., Mobasheri, M., Huete, A., 2014. Evaluating the effect of different wheat rust disease symptoms on vegetation indices using hyperspectral measurements. *Remote Sens.* 6 (6), 5107–5123. <https://doi.org/10.3390/rs6065107>.
- Baral, H.-O., Queloz, V., Hosoya, T., 2014. *Hymenoscyphus fraxineus*, the correct scientific name for the fungus causing ash dieback in Europe. *Int. Mycol. Assoc. Fungus* 79–80.
- Baranowski, P., Jedryczka, M., Mazurek, W., Babula-Skowronska, D., Siedliska, A., Kaczmarek, J., 2015. Hyperspectral and thermal imaging of oilseed rape (*Brassica napus*) response to fungal species of the genus *Alternaria*. *PLoS One* 10 (3), e0122913. <https://doi.org/10.1371/journal.pone.0122913>.
- Barbedo, J., 2019. A review on the use of unmanned aerial vehicles and imaging sensors for monitoring and assessing plant stresses. *Drones* 3 (2), 40. <https://doi.org/10.3390/drones3020040>.
- Barbosa, B.D.S., Araújo e Silva Ferraz, G., Mendes dos Santos, L., Santana, L.S., Bedin Marin, D., Rossi, G., Conti, L., 2021. Application of RGB images obtained by UAV in coffee farming. *Remote Sens.* 13 (12), 2397. <https://doi.org/10.3390/rs13122397>.
- Bendig, J., Yu, K., Aasen, H., Bolten, A., Bennertz, S., Broscheit, J., Gnyp, M.L., Bareth, G., 2015. Combining UAV-based plant height from crop surface models, visible, and near infrared vegetation indices for biomass monitoring in barley. *Int. J. Appl. Earth Obs. Geoinf.* 39, 79–87. <https://doi.org/10.1016/j.jag.2015.02.012>.
- Bhandari, M., Ibrahim, A.M., Xue, Q., Jung, J., Chang, A., Rudd, J.C., Maeda, M., Rajan, N., Neely, H., Landivar, J., 2020. Assessing winter wheat foliage disease severity using aerial imagery acquired from small Unmanned aerial vehicle (UAV). *Comput. Electron. Agric.* 176, 105665. <https://doi.org/10.1016/j.compag.2020.105665>.
- Buchner, L., Eisen, A.-K., Jochner-Oette, S., 2024. Effects of ash dieback on leaf physiology and leaf morphology of *Fraxinus excelsior* L. *Trees*. <https://doi.org/10.1007/s00468-024-02546-1>.
- Buchner, L., Eisen, A.-K., Sikoparija, B., Jochner-Oette, S., 2022. Pollen viability of *Fraxinus excelsior* in storage experiments and investigations on the potential effect of long-range transport. *Forests* 13 (4), 600. <https://doi.org/10.3390/f13040600>.
- Bundesministerium für Ernährung und Landwirtschaft (BMEL) (2024) Der Wald in Deutschland - Ausgewählte Ergebnisse der vierten Bundeswaldinventur.
- Cai, N., Zhou, X., Yang, Y., Wang, J., Zhang, D., Hu, R., 2018. Use of UAV images to assess narrow brown leaf spot severity in rice. *Int. J. Precis. Agric. Aviat.* 1 (1), 38–42. <https://doi.org/10.33440/j.ijpaa.20190202.47>.
- Candiago, S., Remondino, F., Giglio, M. de, Dubbini, M., Gattelli, M., 2015. Evaluating multispectral images and vegetation indices for precision farming applications from UAV images. *Remote Sens.* 7 (4), 4026–4047. <https://doi.org/10.3390/rs70404026>.
- Castro, A.I. de, Shi, Y., Maja, J.M., Peña, J.M., 2021. UAVs for vegetation monitoring: overview and recent scientific contributions. *Remote Sens.* 13 (11), 2139. <https://doi.org/10.3390/rs13112139>.
- Chaerle, L., van Caeneghem, W., Messens, E., Lambers, H., van Montagu, M., van der Straeten, D., 1999. Presymptomatic visualization of plant–virus interactions by thermography. *Nat. Biotechnol.* 17, 813–816.
- Chan, A.H.Y., Barnes, C., Swinfield, T., Coomes, D.A., 2021. Monitoring ash dieback (*Hymenoscyphus fraxineus*) in british forests using hyperspectral remote sensing. *Remote Sens. Ecol. Conserv.* 7 (2), 306–320. <https://doi.org/10.1002/rse2.190>.
- Chang, A., Yeom, J., Jung, J., Landivar, J., 2020. Comparison of canopy shape and vegetation indices of citrus trees derived from UAV multispectral images for characterization of citrus greening disease. *Remote Sens.* 12 (24), 4122. <https://doi.org/10.3390/rs12244122>.
- Chicco, D., Jurman, G., 2020. The advantages of the Matthews correlation coefficient (MCC) over F1 score and accuracy in binary classification evaluation. *BMC Genom.* 21 (1), 6. <https://doi.org/10.1186/s12864-019-6413-7>.
- Choosumrong, S., Hataitara, R., Sujipuli, K., Weerawatanakorn, M., Preechaharn, A., Premjet, D., Laywisadkul, S., Raghavan, V., Panumonwatee, G., 2023. Bananas diseases and insect infestations monitoring using multi-spectral camera RTK UAV images. *Spat. Inf. Res.* 31 (4), 371–380. <https://doi.org/10.1007/s41324-022-00504-y>.
- Coker, T.L.R., Rozsypálek, J., Edwards, A., Harwood, T.P., Buttfoy, L., Buggs, R.J.A., 2019. Estimating mortality rates of European ash (*Fraxinus excelsior*) under the ash dieback (*Hymenoscyphus fraxineus*) epidemic. *Plants People Planet* 1 (1), 48–58. <https://doi.org/10.1002/ppp3.11>.
- Dalpono, M., Reyes, F., Kandare, K., Gianelle, D., 2015. Delineation of individual tree crowns from ALS and hyperspectral data: a comparison among four methods. *Eur. J. Remote Sens.* 48 (1), 365–382. <https://doi.org/10.5721/EuJRS20154821>.
- Dash, J.P., Watt, M.S., Pearse, G.D., Heaphy, M., Dungey, H.S., 2017. Assessing very high resolution UAV imagery for monitoring forest health during a simulated disease outbreak. *ISPRS J. Photogramm. Remote Sens.* 131, 1–14. <https://doi.org/10.1016/j.isprsjprs.2017.07.007>.
- DJI (2022) DJI Mavic 3M User Manual.
- Eisen, A.-K., Buchner, L., Fussi, B., Jochner-Oette, S., 2024. Does ash dieback affect the reproductive ecology of *Fraxinus excelsior* L.? *J. For. Res.* 35 (1). <https://doi.org/10.1007/s11676-023-01670-x>.
- Enderle, R., Fussi, B., Lenz, H.D., Langer, G., Nagel, R., Metzler, B., 2017a. Ash dieback in Germany: research on disease development, resistance and management options. In: Vasaitis, R., Enderle, R. (Eds.), *Dieback of European Ash (Fraxinus spp.) - Consequences and Guidelines for Sustainable Management*. Swedish University of Agricultural Sciences, Uppsala, Sweden, pp. 89–105.
- Enderle, R., Nakou, A., Thomas, K., Metzler, B., 2015. Susceptibility of autochthonous German *Fraxinus excelsior* clones to *Hymenoscyphus pseudoalbidus* is genetically determined. *Ann. For. Sci.* 72 (2), 183–193. <https://doi.org/10.1007/s13595-014-0413-1>.
- Enderle, R., Sander, F., Metzler, B., 2017b. Temporal development of collar necroses and butt rot in association with ash dieback. *iForest* 10 (3), 529–536. <https://doi.org/10.3832/ifor2407-010>.
- Enderle, R., Stenlid, J., Vasaitis, R., 2019. An overview of ash (*Fraxinus* spp.) and the ash dieback disease in Europe. *CABI Rev.* 1–12. <https://doi.org/10.1079/PAVSNNR201914025>.

- Fawcett, T., 2006. An introduction to ROC analysis. *Pattern Recognit. Lett.* 27 (8), 861–874. <https://doi.org/10.1016/j.patrec.2005.10.010>.
- Fachagentur Nachhaltige Rohstoffe e. V. (FNR) (2024) Zukunft der Esche. Empfehlungen zum forstbetrieblichen Umgang mit dem Eschentriebsterben.
- Foody, G.M., 2023. Challenges in the real world use of classification accuracy metrics: from recall and precision to the Matthews correlation coefficient. *PLoS One* 18 (10), e0291908. <https://doi.org/10.1371/journal.pone.0291908>.
- Fuchs, S., Häuser, H., Peters, S., Knauf, L., Rentschler, F., Kahlenberg, G., Kätzel, R., Evers, J., Paar, U., Langer, G.J., 2024. Ash dieback assessments on intensive monitoring plots in Germany: influence of stand, site and time on disease progression. *J. Plant Dis. Prot.* <https://doi.org/10.1007/s41348-024-00889-y>.
- Garza, B.N., Ancona, V., Enciso, J., Perotto-Baldovino, H.L., Kunta, M., Simpson, C., 2020. Quantifying citrus tree health using true color UAV images. *Remote Sens.* 12 (1), 170. <https://doi.org/10.3390/rs12010170>.
- Granum, E., Pérez-Bueno, M.L., Calderón, C.E., Ramos, C., Vicente, A. de, Cazorla, F.M., Barón, M., 2015. Metabolic responses of avocado plants to stress induced by *Rosellinia necatrix* analysed by fluorescence and thermal imaging. *Eur. J. Plant Pathol.* 142 (3), 625–632. <https://doi.org/10.1007/s10658-015-0640-9>.
- Guo, A., Huang, W., Dong, Y., Ye, H., Ma, H., Liu, B., Wu, W., Ren, Y., Ruan, C., Geng, Y., 2021. Wheat yellow rust detection using UAV-based hyperspectral technology. *Remote Sens.* 13 (1), 123. <https://doi.org/10.3390/rs13010123>.
- Harrap, M.J.M., Hempel de Ibarra, N., Whitney, H.M., Rands, S.A., 2018. Reporting of thermography parameters in biology: a systematic review of thermal imaging literature. *R. Soc. Open Sci.* 5 (12), 181281. <https://doi.org/10.1098/rsos.181281>.
- Hashim, I.C., Shariff, A.R.M., Bejo, S.K., Muharam, F.M., Ahmad, K., Hashim, H., 2020. Application of thermal imaging for plant disease detection. *IOP Conf. Ser. Earth Environ. Sci.* 540 (1), 12052. <https://doi.org/10.1088/1755-1315/540/1/012052>.
- Holzwarth, S., Thonfeld, F., Kacic, P., Abdullahi, S., Asam, S., Coleman, K., Eisfeldner, C., Gessner, U., Huth, J., Kraus, T., Shatto, C., Wessel, B., Kuenzer, C., 2023. Earth-observation-based monitoring of forests in Germany—recent progress and research frontiers: a review. *Remote Sens.* 15 (17), 4234. <https://doi.org/10.3390/rs15174234>.
- Huete, A.R., 2012. Vegetation indices, remote sensing and forest monitoring. *Geogr. Compass* 6 (9), 513–532. <https://doi.org/10.1111/j.1749-8198.2012.00507.x>.
- Hultberg, T., Sandström, J., Felton, A., Öhman, K., Rönnerberg, J., Witzell, J., Cleary, M., 2020. Ash dieback risks an extinction cascade. *Biol. Conserv.* 244, 108516. <https://doi.org/10.1016/j.biocon.2020.108516>.
- Jafari, M., Minaei, S., Safaie, N., 2017. Detection of pre-symptomatic rose powdery-mildew and gray-mold diseases based on thermal vision. *Infrared Phys. Technol.* 85, 170–183. <https://doi.org/10.1016/j.infrared.2017.04.023>.
- James, G., Witten, D., Hastie, T., Tibshirani, R., Taylor, J., 2023. *An Introduction to Statistical Learning*. Springer International Publishing, Cham.
- Jie, P., Heng, Z., Yunwei, J., Zhenfeng, L., 2015. Early monitoring of pine wilt disease in *Pinus massoniana* based on hyperspectral data. *Plant Dis. Pests* 6 (4–5), 1–5.
- Kampen, M., Lederbauer, S., Mund, J.-P., Immitzer, M., 2019. UAV-based multispectral data for tree species classification and tree vitality analysis. Dreiländertagung der DGPF, der OOVG und der SGPF in Wien. Österreich (28).
- Kattenborn T. (2023) DJI thermal rpeg to tif (v. 0.5). ([https://github.com/tejakattenborn/dji\\_h20t\\_rpeg\\_to\\_tif](https://github.com/tejakattenborn/dji_h20t_rpeg_to_tif)).
- Kleinsmann, J., Verbesselt, J., Koistra, L., 2023. Monitoring individual tree phenology in a multi-species forest using high resolution UAV images. *Remote Sens.* 15 (14), 3599. <https://doi.org/10.3390/rs15143599>.
- Kowalski, T., 2006. *Chalara fraxinea* sp. nov. associated with dieback of ash (*Fraxinus excelsior*) in Poland. *For. Pathol.* 36, 264–270. <https://doi.org/10.1111/j.1439-0329.2006.00453.x>.
- Leblanc, G., Kalacska, M., Arroyo-Mora, J.P., Lucanus, O., Todd, A., 2021. A practical validation of uncooled thermal imagers for small RPAS. *Drones* 5 (4), 132. <https://doi.org/10.3390/drones5040132>.
- Lee, S., Pradhan, B., 2007. Landslide hazard mapping at Selangor, Malaysia using frequency ratio and logistic regression models. *Landslides* 4 (1), 33–41. <https://doi.org/10.1007/s10346-006-0047-y>.
- Lenz, H., Straßer, L., Baumann, M., Baier, U., 2012. Boniturschlüssel zur Einstufung der Vitalität von Alteschen. *AFZ-DerWald* 18–19.
- Lindenthal, M., Steiner, U., Dehne, H.-W., Oerke, E.-C., 2005. Effect of downy mildew development on transpiration of cucumber leaves visualized by digital infrared thermography. *Am. Phytopathol. Soc.* 95 (3), 233–240. <https://doi.org/10.1094/PHYTO-95-0233>.
- Lussem, U., Bolten, A., Gny, M.L., Jasper, J., Bareth, G., 2018. Evaluation of RGB-based vegetation indices from UAV imagery to estimate forage yield in grassland. *Int. Arch. Photogramm. Remote Sens. Spat. Inf. Sci. XLII-3*, 1215–1219. <https://doi.org/10.5194/isprs-archives-XLII-3-1215-2018>.
- Mahlein, A.-K., Rumpf, T., Welke, P., Dehne, H.-W., Plümer, L., Steiner, U., Oerke, E.-C., 2013. Development of spectral indices for detecting and identifying plant diseases. *Remote Sens. Environ.* 128, 21–30. <https://doi.org/10.1016/j.rse.2012.09.019>.
- Malbêteau, Y., Johansen, K., Aragon, B., Al-Mashhawari, S.K., McCabe, M.F., 2021. Overcoming the challenges of thermal infrared orthomosaics using a swath-based approach to correct for dynamic temperature and wind effects. *Remote Sens.* 13 (16), 3255. <https://doi.org/10.3390/rs13163255>.
- McKinney, L.V., Nielsen, L.R., Hansen, J.K., Kjær, E.D., 2011. Presence of natural genetic resistance in *Fraxinus excelsior* (Oleraceae) to *Chalara fraxinea* (Ascomycota): an emerging infectious disease. *Heredity* 106 (5), 788–797. <https://doi.org/10.1038/hdy.2010.119>.
- Metzler, B., Herbstritt, S., 2014. Sicherheitsrisiko durch Stammfußnekrosen an Eschen, insbesondere auf Nasstandorten. *FVA Waldschutz-INFO*.
- Miraki, M., Sohrabi, H., Fatehi, P., Kneubuehler, M., 2021. Individual tree crown delineation from high-resolution UAV images in broadleaf forest. *Ecol. Inf.* 61, 101207. <https://doi.org/10.1016/j.ecoinf.2020.101207>.
- Mitchell, R.J., Broome, A., Beaton, J.K., Bellamy, P.E., Ellis, C.J., Hester, A.J., Hodgetts, N.G., Iason, G.R., Littlewood, N.A., Newey, S., Pozsgai, G., Ramsay, S., Riach, D., Stockan, J.A., Taylor, A.F.S., Woodward, S., 2017. Challenges in assessing the ecological impacts of tree diseases and mitigation measures: the case of *Hymenoscyphus fraxineus* and *Fraxinus excelsior*. *Balt. For.* 23 (1), 116–140.
- Mohan, M., Silva, C., Klauberg, C., Jat, P., Catts, G., Cardil, A., Dia, M., 2017. Individual tree detection from unmanned aerial vehicle (UAV) derived canopy height model in an open canopy mixed conifer forest. *Forests* 8 (9), 340. <https://doi.org/10.3390/f8090340>.
- Murfit, J., He, Y., Yang, J., Mui, A., Mille, K. de, 2016. Ash decline assessment in emerald ash borer infested natural forests using high spatial resolution images. *Remote Sens.* 8 (3), 256. <https://doi.org/10.3390/rs8030256>.
- Neupane, K., Baysal-Gurel, F., 2021. Automatic identification and monitoring of plant diseases using unmanned aerial vehicles: a review. *Remote Sens.* 13 (19), 3841. <https://doi.org/10.3390/rs13193841>.
- Ortiz-Bustos, C.M., Pérez-Bueno, M.L., Barón, M., Molinero-Ruiz, L., 2017. Use of blue-green fluorescence and thermal imaging in the early detection of sunflower infection by the root parasitic weed *Orobancha cumana* Wallr. *Front. Plant Sci.* 8, 833. <https://doi.org/10.3389/fpls.2017.00833>.
- Otsu, K., Pla, M., Duane, A., Cardil, A., Brotons, L., 2019. Estimating the threshold of detection on tree crown defoliation using vegetation indices from UAS multispectral imagery. *Drones* 3 (4), 80. <https://doi.org/10.3390/drones3040080>.
- Panagiotidis, D., Abdollahnejad, A., Surový, P., Chirculeu, V., 2017. Determining tree height and crown diameter from high-resolution UAV imagery. *Int. J. Remote Sens.* 38 (8–10), 2392–2410. <https://doi.org/10.1080/01431161.2016.1264028>.
- Park, J., Muller-Landau, H., Lichstein, J., Rifai, S., Dandois, J., Bohlman, S., 2019. Quantifying leaf phenology of individual trees and species in a tropical forest using Unmanned Aerial Vehicle (UAV) images. *Remote Sens.* 11 (13), 1534. <https://doi.org/10.3390/rs11131534>.
- Pautasso, M., Aas, G., Queloz, V., Holdenrieder, O., 2013. European ash (*Fraxinus excelsior*) dieback – a conservation biology challenge. *Biol. Conserv.* 158, 37–49. <https://doi.org/10.1016/j.biocon.2012.08.026>.
- Peters, S., Langer, G., Kätzel, R. (Eds.), 2021. *Eschentriebsterben. Kriterien zur Schadensbonitur an Eschen, 1. Auflage*. Fachagentur Nachhaltige Rohstoffe (FNR), Gülzow-Prützen.
- Poblete, T., Camino, C., Beck, P., Hornero, A., Kattenborn, T., Saponari, M., Boscia, D., Navas-Cortes, J.A., Zarco-Tejada, P.J., 2020. Detection of *Xylella fastidiosa* infection symptoms with airborne multispectral and thermal imagery: assessing bandset reduction performance from hyperspectral analysis. *ISPRS J. Photogramm. Remote Sens.* 162, 27–40. <https://doi.org/10.1016/j.isprsjprs.2020.02.010>.
- Polk, S.L., Chan, A.H.Y., Cui, K., Plemmons, R.J., Coomes, D.A., Murphy, J.M., 2022. Unsupervised detection of ash dieback disease (*Hymenoscyphus fraxineus*) using diffusion-based hyperspectral image clustering. *IGARSS 2022 - 2022 IEEE Int. Geosci. Remote Sens. Symp.* 2287–2290. <https://doi.org/10.1109/IGARSS46834.2022.9883429>.
- Pontius, J., Martin, M., Plourde, L., Hallett, R., 2008. Ash decline assessment in emerald ash borer-infested regions: a test of tree-level, hyperspectral technologies. *Remote Sens. Environ.* 112 (5), 2655–2676. <https://doi.org/10.1016/j.rse.2007.12.011>.
- Qiu, L., Jing, L., Hu, B., Li, H., Tang, Y., 2020. A new individual tree crown delineation method for high resolution multispectral imagery. *Remote Sens.* 12 (3), 585. <https://doi.org/10.3390/rs12030585>.
- Raza, S.-A., Prince, G., Clarkson, J.P., Rajpoot, N.M., 2015. Automatic detection of diseased tomato plants using thermal and stereo visible light images. *PLoS One* 10 (4), e0123262. <https://doi.org/10.1371/journal.pone.0123262>.
- Sansechan, P., Saengprachathanarug, K., Posom, J., Wongpichet, S., Chea, C., Wongphat, M., 2019. Use of vegetation indices in monitoring sugarcane white leaf disease symptoms in sugarcane field using multispectral UAV aerial imagery. *IOP Conf. Ser. Earth Environ. Sci.* 301 (1), 12025. <https://doi.org/10.1088/1755-1315/301/1/012025>.
- Skovsgaard, J.P., Wilhelm, G.J., Thomsen, I.M., Metzler, B., Kirisits, T., Havrdová, L., Enderle, R., Dobrowska, D., Cleary, M., Clark, J., 2017. Silvicultural strategies for *Fraxinus excelsior* in response to dieback caused by *Hymenoscyphus fraxineus*. *For. Int. J. For. Res.* 90 (4), 455–472. <https://doi.org/10.1093/forestry/cpx012>.
- Smigaj, M., Gaulton, R., Barr, S.L., Suárez, J.C., 2015. UAV-borne thermal imaging for forest health monitoring: detection of disease-induced canopy temperature increase. *Int. Arch. Photogramm. Remote Sens. Spat. Inf. Sci. XL-3/W3*, 349–354. <https://doi.org/10.5194/isprsarchives-XL-3-W3-349-2015>.
- Starý, K., Jelínek, Z., Kumlálová, J., Chyba, J., Balázová, K., 2020. Comparing RGB-based vegetation indices from UAV imagery to estimate hops canopy area. *10.15159/AR.20.169*.
- Steddom, K., Bredhoeft, M.W., Khan, M., Rush, C.M., 2005. Comparison of visual and multispectral radiometric disease evaluations. *Plant Dis.* 153–158. <https://doi.org/10.1094/PD-89-0153>.
- Suh, H.K., Hofstee, J.W., van Henten, E.J., 2020. Investigation on combinations of colour indices and threshold techniques in vegetation segmentation for volunteer potato control in sugar beet. *Comput. Electron. Agric.* 179, 105819. <https://doi.org/10.1016/j.compag.2020.105819>.
- Timmermann, V., Borja, I., Hietala, A.M., Kirisits, T., Solheim, H., 2011. Ash dieback: pathogen spread and diurnal patterns of ascospore dispersal, with special emphasis on Norway. *OEPP/Eppo Bull.* 41, 14–20. <https://doi.org/10.1111/j.1365-2338.2010.02429.x>.
- Torresan, C., Berton, A., Carotenuto, F., Di Gennaro, S.F., Gioli, B., Matese, A., Miglietta, F., Vagnoli, C., Zaldei, A., Wallace, L., 2017. Forestry applications of UAVs

- in Europe: a review. *Int. J. Remote Sens.* 38 (8-10), 2427–2447. <https://doi.org/10.1080/01431161.2016.1252477>.
- Torres-Sánchez, J., Peña, J.M., Castro, A.I. de, López-Granados, F., 2014. Multi-temporal mapping of the vegetation fraction in early-season wheat fields using images from UAV. *Comput. Electron. Agric.* 103, 104–113. <https://doi.org/10.1016/j.compag.2014.02.009>.
- Vilela, E.F., Da Silva, C.A., Botti, J.M.C., Martins, E.F., Santana, C.C., Marin, D.B., Freitas, A.Rd.J., Jaramillo-Giraldo, C., Lopes, I.Pd.C., Corrêdo, Ld.P., Queiroz, D.M. de, Rossi, G., Bambi, G., Conti, L., Venzon, M., 2024. Detection of coffee leaf miner using RGB aerial imagery and machine learning. *AgriEngineering* 6 (3), 3174–3186. <https://doi.org/10.3390/agriengineering6030181>.
- Waser, L., Küchler, M., Jütte, K., Stampfer, T., 2014. Evaluating the potential of worldview-2 data to classify tree species and different levels of ash mortality. *Remote Sens.* 6 (5), 4515–4545. <https://doi.org/10.3390/rs6054515>.
- Wu, D., Yu, L., Yu, R., Zhou, Q., Li, J., Zhang, X., Ren, L., Luo, Y., 2023. Detection of the monitoring window for pine wilt disease using multi-temporal UAV-based multispectral imagery and machine learning algorithms. *Remote Sens.* 15 (2), 444. <https://doi.org/10.3390/rs15020444>.
- Xue, J., Su, B., 2017. Significant remote sensing vegetation indices: a review of developments and applications. *J. Sens.* 2017, 1–17. <https://doi.org/10.1155/2017/1353691>.
- Yadav, S., Shukla, S., 2016. Analysis of k-Fold cross-validation over hold-out validation on colossal datasets for quality classification. 2016 IEEE 6th Int. Conf. Adv. Comput. (IACC) 78–83. <https://doi.org/10.1109/IACC.2016.25>.
- Ye, H., Huang, W., Huang, S., Cui, B., Dong, Y., Guo, A., Ren, Y., Jin, Y., 2020. Recognition of banana Fusarium wilt based on UAV remote sensing. *Remote Sens.* 12 (6), 938. <https://doi.org/10.3390/rs12060938>.
- Zhang, J., Virk, S., Porter, W., Kenworthy, K., Sullivan, D., Schwartz, B., 2019. Applications of unmanned aerial vehicle based imagery in turfgrass field trials. *Front. Plant Sci.* 10, 279. <https://doi.org/10.3389/fpls.2019.00279>.